ACS APPLIED BIO MATERIALS

Article

Cite This: ACS Appl. Bio Mater. 2018, 1, 79−89

www.acsabm.org

T_1- and T_2-weighted Magnetic Resonance Dual Contrast by Single Core Truncated Cubic Iron Oxide Nanoparticles with Abrupt Cellular Internalization and Immune Evasion

Bibek Thapa,[*,†,‡] Daysi Diaz-Diestra,[†,∥] Carlene Santiago-Medina,[†,⊥] Nitu Kumar,[†] Kaixiong Tu,[∥] Juan Beltran-Huarac,[*,†,§] Wojciech M. Jadwisienczak,[¶] Brad R. Weiner,[†,∥] and Gerardo Morell[†,‡]

[†]Molecular Sciences Research Center, University of Puerto Rico, San Juan, Puerto Rico 00926-2614, United States

[‡]Department of Physics, University of Puerto Rico, Río Piedras Campus, San Juan, Puerto Rico 00925-2537, United States

[∥]Department of Chemistry, University of Puerto Rico, Río Piedras Campus, San Juan, Puerto Rico 00925-2537, United States

[⊥]Department of Biology, University of Puerto Rico, Río Piedras Campus, San Juan, Puerto Rico 00925-2537, United States

[§]Department of Environmental Health, Harvard University, Boston, Massachusetts 02115-5810, United States

[¶]School of Electrical Engineering and Computer Science, Ohio University, Athens, Ohio 45701-2769, United States

Supporting Information

ABSTRACT: Conventional T_1- or T_2-weighted single mode contrast-enhanced magnetic resonance imaging (MRI) may produce false results. Thereby, there is a need to develop dual contrast agents, T_1- and T_2-weighted, for more accurate MRI imaging. The dual contrast agents should possess high magnetic resonance (MR) relaxivities, targeted tumor linking, and minimum recognition by the immune system. We have developed nitrodopamine-PEG grafted single core truncated cubic iron oxide nanoparticles (ND-PEG-tNCIOs) capable of producing marked dual contrasts in MRI with enhanced longitudinal and transverse relaxivities of 32 ± 1.29 and 791 ± 38.39 mM^{-1} s^{-1}, respectively. Furthermore, the ND-PEG-tNCIOs show excellent colloidal stability in physiological buffers and higher cellular internalization in cancerous cells than in phagocytic cells, indicating the immune evasive capability of the nanoparticles. These findings indicate that tNCIOs are strong candidates for dual contrast MRI imaging, which is vital for noninvasive real-time detection of nascent cancer cells in vivo and for monitoring stem cells transplants.

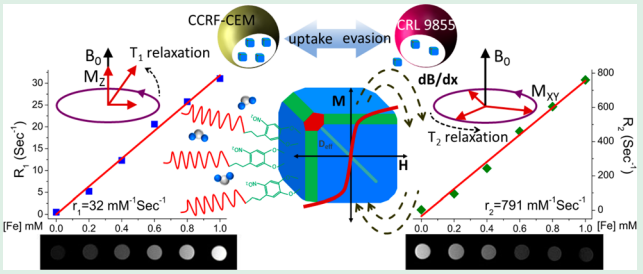

KEYWORDS: *magnetic resonance imaging, T_1- and T_2-weighted dual contrast, longitudinal and transverse relaxivity, truncated cubic iron oxide nanoparticles, cellular internalization, immune evasion*

INTRODUCTION

Since its invention over three and half decades ago, magnetic resonance imaging (MRI) has become an indispensable technology in the field of medical diagnostics. It is a broadly deployed clinical imaging modality, which enables noninvasive observation of anatomy and function at the cellular and molecular scale with high-spatial and temporal resolution.[1] Clinical magnetic resonance (MR) examinations can require intravenous contrast agents (CAs) to enhance the sensitivity and specificity of diagnosis. Indeed, about one-third of the 60 million annual worldwide MRI producers employ CAs in MRI procedures.[2] There are four major classes of MRI CAs: (i) water protons' relaxation-based T_1 and T_2, (ii) T_2 exchange (T_{2ex}), (iii) chemical exchange saturation transfer (CEST), and (iii) hyperpolarized ^{13}C CAs.[3] Among these classes, water protons' relaxation-based T_1 and T_2, such as paramagnetic gadolinium (Gd)-based and superparamagnetic iron oxide nanoparticles CAs, are the most widely used for anatomical imaging.[4]

Radiologists favor T_1 CAs over T_2 CAs since the latter may lead to an erroneous diagnosis due to an intrinsic blurred dark signal in hypointense areas, i.e., bleeding, calcification, or metal deposition.[5] The currently used paramagnetic gadolinium (Gd)-based T_1 CAs, however, produce adverse effects in patients with severe nephrogenic systemic fibrosis (NSF) causing impaired renal function[6] and long-term deposition of Gd in the human brain.[7,8] More specifically, the gadolinium chelates have a short lifetime in blood that limits the available imaging window and rapidly distribute into the extravascular space reducing the signal-to-background contrast.[9] Because of these limitations, the development of a benign alternative to Gd-based CAs is a pressing concern.

Recently, there have been several reports on the safety of superparamagnetic iron oxide nanoparticles. Ferumoxytol (i.e.,

Received: April 21, 2018
Accepted: June 15, 2018
Published: June 15, 2018

DOI: 10.1021/acsabm.8b00016
ACS Appl. Bio Mater. 2018, 1, 79−89

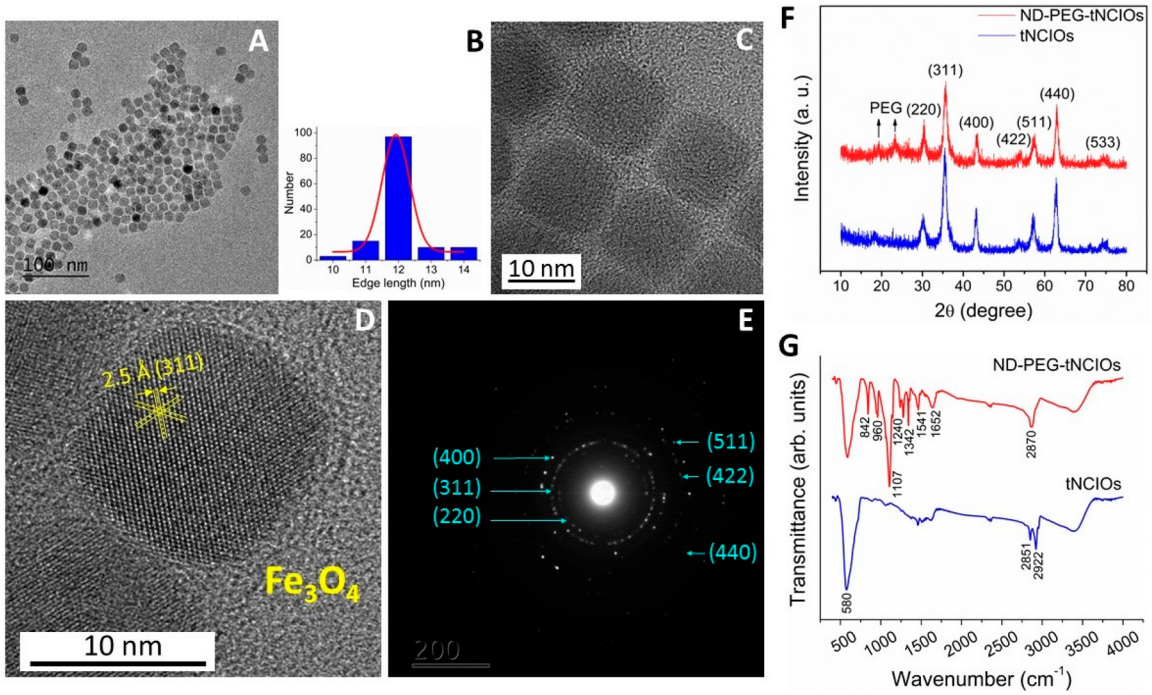

Figure 1. (A) TEM image of as-synthesized oleic acid-coated tNCIOs (scale bar: 10 nm). (B) Size distribution profile of tNCIOs and Gaussian fitting, as seen from the TEM image. (C, D) High-resolution TEM (HRTEM) images of tNCIO. (E) Selected area electron diffraction (SAED) patterns. (F) Powder XRD patterns and (G) ATR-FTIR spectra of tNCIOs and ND-PEG-tNCIOs.

Feraheme injection, AMAG Pharmaceuticals), a polyglucose sorbitol carboxymethyl ether-coated superparamagnetic iron oxide nanoparticle, has shown minimal tendency to release free iron atoms as compared to clinically available iron preparations.[10] Similarly, Ferumoxytol has been applied intravenously to treat anemia in adult patients with chronic kidney disease[11,12] for more than a decade. Iron oxide nanoparticles are assimilated in the human body through iron metabolism, DNA synthesis, and red blood cells production[13] and are stored as ferritin causing minimal harm to human health.[14] Consequently, the iron oxide-based CAs can be a safer alternative to Gd-based CAs. Thus, it is imperative to develop either superparamagnetic iron oxide nanoparticles with enhanced transverse (r_2) relaxivity to minimize the erroneous diagnosis, or paramagnetic iron oxide nanoparticles with enhanced longitudinal (r_1) relaxivity. Regarding to this fact, there are numerous reports on the development of anisotropic-shaped superparamagnetic iron oxide nanoparticles as T_2 CAs[15−17] as well as their ultralow dimensional counterparts as T_1 CAs.[2,18] However, the conventional T_1- or T_2-weighted single imaging modality results in false imaging, particularly in calcified tissues,[19] and hence, the concern on the dual-imaging T_1-and T_2-weighted modality is escalating.

The superparamagnetic and paramagnetic hybrid systems[20,21] and the dumbbell-hybrid nanotrimers (DB-HNTs) consisting of iron oxide and gold nanoparticles[22] were reported showing dual contrasts in MRI. However, the synthesis of such materials is arduous and cumbersome. Gong et al. reported enhanced dual contrasts using a manganese ferrite ($MnFe_3O_4$) nanoparticle assembly,[23] but the manganese ions administered to the human body may result in neurotoxicity and cellular toxicity.[24,25] Similarly, Zhou et al. demonstrated synergistic enhancement of dual MR contrasts using gadolinium oxide (Gd_2O_3)-embedded iron oxide (GdIO) nanoparticles;[26] however, the Gd ions can lead to kidney malfunction.[7] Further, sub-10 nm iron oxide nanoparticles have been employed for the dual contrasts in MRI,[27−29] but they exhibit poor longitudinal (r_1) and transverse relaxivity (r_2). In this study, we developed single core tNCIOs capable of enhancing the MRI dual relaxivities and in vitro T_1- and T_2-weighted MRI dual contrasts. The enhanced relaxivities and contrasts are ascribed to effects of the truncated crystal facets of tNCIOs, surface chemistry, effective size, and core magnetization of tNCIOs.

RESULTS AND DISCUSSION

Morphology and Crystallographic Phases. The morphology and crystallographic phases of oleic acid (OA)-coated tNCIOs were characterized using TEM (see Figure 1A,C,D). The as-synthesized oleic acid-coated tNCIOs are discretely assembled (Figure 1A), and the size distribution profile (Figure 1B) shows that the average edge length is ∼12 nm (calculated using ImageJ software, https://imagej.nih.gov/ij/). The monodisperse tNCIOs are evident and indicate the formation of truncated cubic shapes (Figure 1C). The high-resolution TEM (HRTEM) image shows lattice fringes with the characteristic spacing of (311) planes corresponding to the magnetite (Fe_3O_4) phase (Figure 1D). The selected area electron diffraction (SAED) patterns (Figure 1E) show noticeable dotted rings suggesting the formation of polycrystalline tNCIOs with a ring spacing consistent with a typical cubic inverse spinel structure ($Fd3m$), which is characteristic of the magnetite (Fe_3O_4) phase.[30] Furthermore, this phase formation is well-supported by the powder XRD patterns (Figure 1F), which exhibit the typical diffraction peaks of Fe_3O_4[31−33] (JCPDS file no. 79-0418). No other diffraction patterns are observed, suggesting the absence of the contamination.

ATR−FTIR spectroscopy was employed to identify the materials contained in pure tNCIOs and ND-PEG-tNCIOs. According to FTIR transmittance spectra (Figure 1G), the

DOI: 10.1021/acsabm.8b00016
ACS Appl. Bio Mater. 2018, 1, 79−89

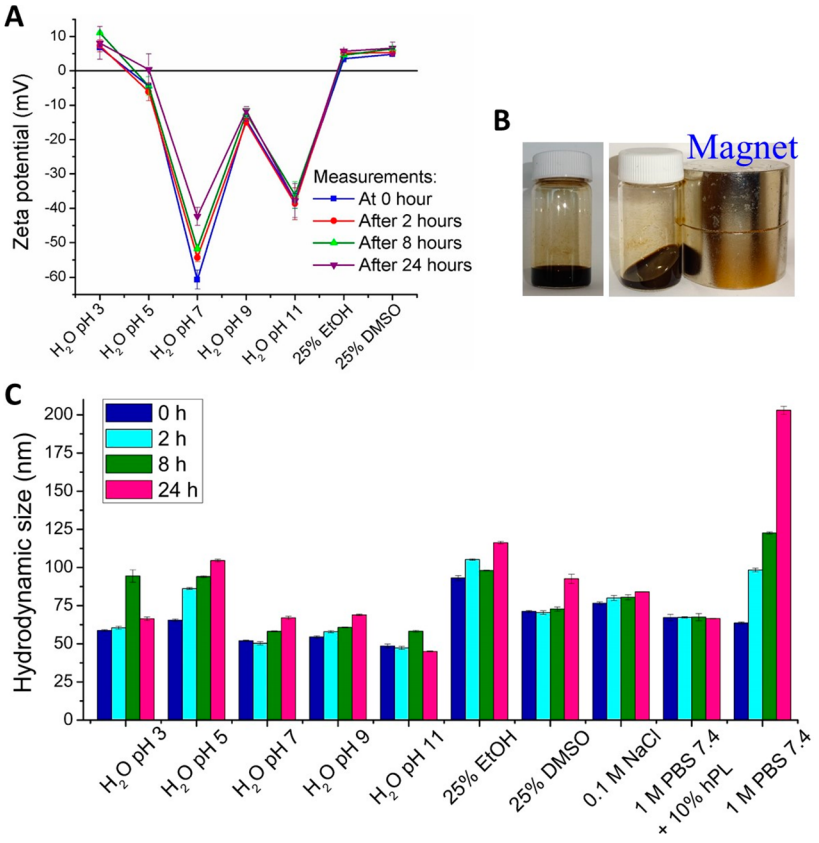

Figure 2. (A) ζ potential measurements of ND-PEG-tNCIOs. (B) Optical image of fluidal form of ND-PEG-tNCIOs (10 mg of ND-PEG-tNCIOs dispersed in 3 mL of deionized water) with and without a magnet. (C) DLS data of ND-PEG-tNCIOs in different media. The measurements were taken at 0 h (fresh sample), 2 , 8, and 24 h.

characteristic band associated with the Fe−O stretching vibration of Fe_3O_4 is observed at 580 cm^{-1}. The well-defined transmittance bands associated with C−O/C−C stretching vibrations and ethylene glycol CH_2 are observed in the range from 842 to 1107 cm^{-1} and from 1240 to 1342 cm^{-1}, respectively. The C═O stretching vibration and the NH deformation vibration of the secondary amide observed at 1652 and 1541 cm^{-1}, respectively, indicate the successful coupling of ND to PEG and the presence of coupled ND-PEG onto the IOs surface. No band related to the residual free PEG uncoupled to ND is observed. The bands seen in the range from 2800 to 3000 cm^{-1} are ascribed to the C−H stretching vibration. These results agree with the results reported previously.[34]

Thermal Properties. The thermogravimetry (TG) and differential scanning calorimetry (DSC) were performed to study the thermal properties of the samples (Figure S1 in the Supporting Information). The TG profile of tNCIOs (Figure S1A) shows a marginal weight loss in the first step until 160 °C, which is characteristic of the evaporation of water molecules from the surface of the sample. Furthermore, a two-step weight loss from 160 to 350 °C can be attributed to the loss of adsorbed organic species, e.g., residual oleic acid (OA), and the crystallization to the oxides.[35] A subtle broad exothermic peak in the DSC profile, extending from 220 to 310 °C and centered at 265 °C, corresponds to this crystallization temperature. The steady weight loss beyond 350 °C is indicative of oxidation of the magnetite (Fe_3O_4) phase of tNCIOs to hematite (Fe_2O_3).[36] Figure S1B shows one-step TG and DSC profiles of ND-PEG-tNCIOs. The 30% weight loss between 200 and 325 °C is attributed to the loss of the capping agent and the PEG moieties profile. The weight loss also corresponds to the exothermic peak centered at 287 °C in the DSC profile. The observed one-step TG profile suggests the high purity of the sample. We have calculated the grafting density of the ND-PEG chain based on this weight loss percentage, which resulted to be ∼4 chains per nm^2 (in the Supporting Information).

Hydrodynamic Sizes and Colloidal Properties. The ligand functionalization aims to prevent nanoparticle (NP) aggregation and maintain colloidal stability in the physiological buffers,[37] and hence to enhance the biocompatibility, blood circulation time, and tumor targeting efficacy, which are the fundamental requirements for in vivo imaging and delivery applications of NPs.[38] Nitrodopamine (ND) has double oxygen (−O) functionalities to anchor on the surface of tNCIOs, which can provide steric stabilization in buffers. The ND-PEG-tNCIOs show excellent colloidal stability in different physiological media as evident from the ζ potential measurements, shown in Figure 2A. The optical images (Figure 2B) depict the fluidal form of ND-PEG-tNCIOs dispersed in deionized (DI) water in the absence and presence of an external magnetic field. Figure S2 (in the Supporting Information) shows well-dispersed ND-PEG-tNCIOs in different solvents. In H_2O at pH 7, they exhibit the highest colloidal stability with the ζ potential value of −61 mV, which reduces to −43 mV after 24 h. The high grafting density and the long chain of PEG (mol wt = 5 KDa) screen the van der Waals and the magnetic dipole forces of attractions of the tNCIOs, thereby establishing a high steric repulsion and colloidal

DOI: 10.1021/acsabm.8b00016
ACS Appl. Bio Mater. 2018, 1, 79−89

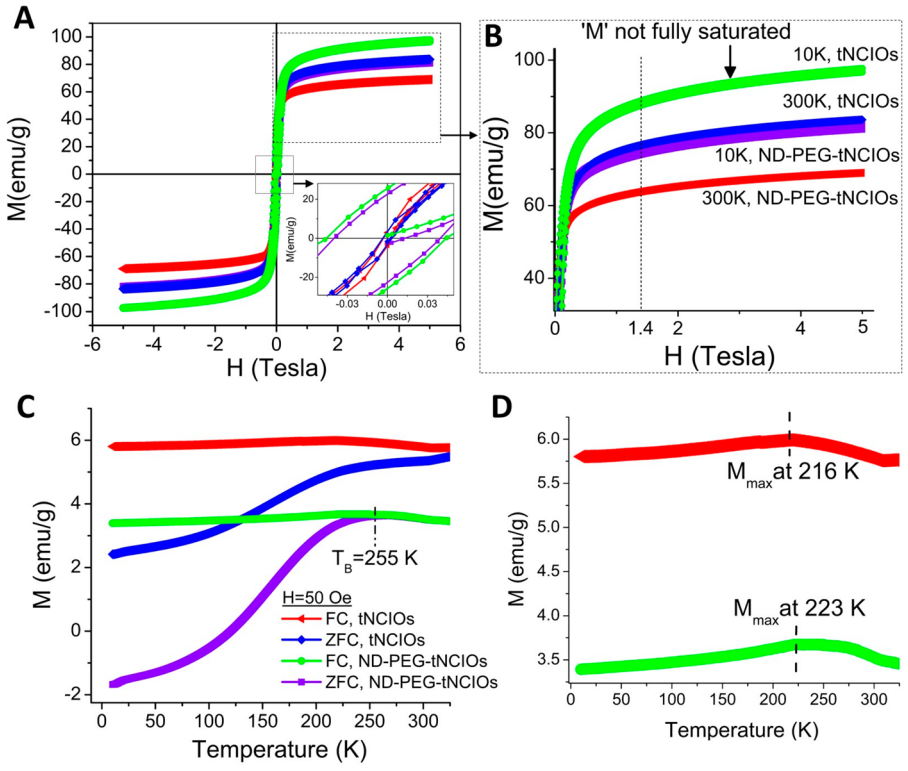

Figure 3. (A) Hysteresis $M(H)$ loops (inset: magnification of $M(H)$ at a low field region). (B) Magnification of the saturation region of panel A. (C) $M(T)$ curves: field-cooled (FC) and zero field-cooled (ZFC) magnetization curves. (D) Magnification of the FC magnetization curves of panel C.

stability. The reduced remnant magnetization (M_R) at the superparamagnetic state can also minimize the magnetic dipole force of attraction among the nanoparticles contributing to their colloidal stability. However, the steric force is difficult to predict and quantify. The surface charges decrease as the acidity increases and acquire the positive charges with the ζ potential of +6 mV. The isoelectric point (IEP) is found to be 4.3, signifying that at this pH value the colloidal system is least stable.[39] Several studies have also reported the negative ζ potentials of the functionalized iron oxide nanoparticles over the basic to the acidic range with an IEP at a lower pH.[40] Further, in the basic condition, the negative charges slightly diminish.

The hydrodynamic size (D_{hyd}) of the nanoparticles is one of the defining parameters in biological applications. The observed D_{hyd} of tNCIOs and ND-PEG-tNCIOs is 53−74 nm in H_2O, pH 7, at 0−24 h. This increase in size is due to the surface coating of ND-PEG (Figure 2C). At lower pH values, the increase in D_{hyd} could be due to desorption of ND-PEG that facilitates the nanoparticles agglomeration via van der Waals and magnetic dipole attractions. Such effects were reported under the basic condition for the citric acid-coated/PEGylated iron oxide nanoparticles.[41] We observed that the D_{hyd} remained less than 100 nm in most media for 2−6 h, which is an appropriate size to avoid renal and hepatic clearance[42] in vivo and to improve drug delivery through an enhanced permeation and retention (EPR) effect.

Magnetic Properties. The magnetic properties of the iron oxide nanoparticles are strongly dependent on their shape, size, and crystallinity.[43] We have performed magnetic field- and temperature-dependent magnetic measurements in PPMS using a VSM technique. Figure 3A shows the mass magnetization (emu/g) versus applied magnetic field (Tesla) curves [M(H) hysteresis loops] for both samples measured in the range of ±5 T at 300 and 10 K. The tNCIOs exhibit saturation magnetization (M_S) of 77 emu/g of "Fe" at 300 K, which increased to 90 emu/g at 10 K while the ND-PEG-tNCIOs show M_S of 66 and 75 emu/g at 300 and 10 K, respectively. Smolensky et al. reported that the anchoring groups with catechol functionalities can retain the saturation magnetization and relaxivity of iron oxide nanoparticles more efficiently than the carboxylate and phosphonate groups.[44] Due to this significance of catechol group, we chose ND as the anchoring group in this study. The decrease in M_S after functionalization is indicative of the spin canting effect due to the magnetically dead layer of ND-PEG,[31] while the increased anisotropy energy at low temperatures enables the magnetic correlation between surface spins via exchange coupling, increasing the M_S at 10 K.[45] It is also evident that the decreased magnetic field is not sufficient to disturb the alignment of spins along the anisotropic easy axis at low temperatures, which affords enhanced remanence (M_R) and coercivity (H_C), thus yielding ferromagnetism. At 300 K, the thermal energy overcomes the anisotropy energy giving faster Néel relaxation than the measurement time and hence facilitates the easy flip of the spins bearing superparamagnetism.

The high-resolution $M(H)$ hysteresis loops in Figure 3B show that the magnetization of the nanoparticles does not accomplish full saturation as the magnetization progresses from the dynamic to saturation region. For the low dimensional regime of an edge length of 12 nm, the tNCIOs acquire a large number of canted spins on their surface. These canted spins preclude achieving the full saturation, showing a subtle paramagnetic behavior in the nanoparticles. A cubic nano-

DOI: 10.1021/acsabm.8b00016
ACS Appl. Bio Mater. 2018, 1, 79−89

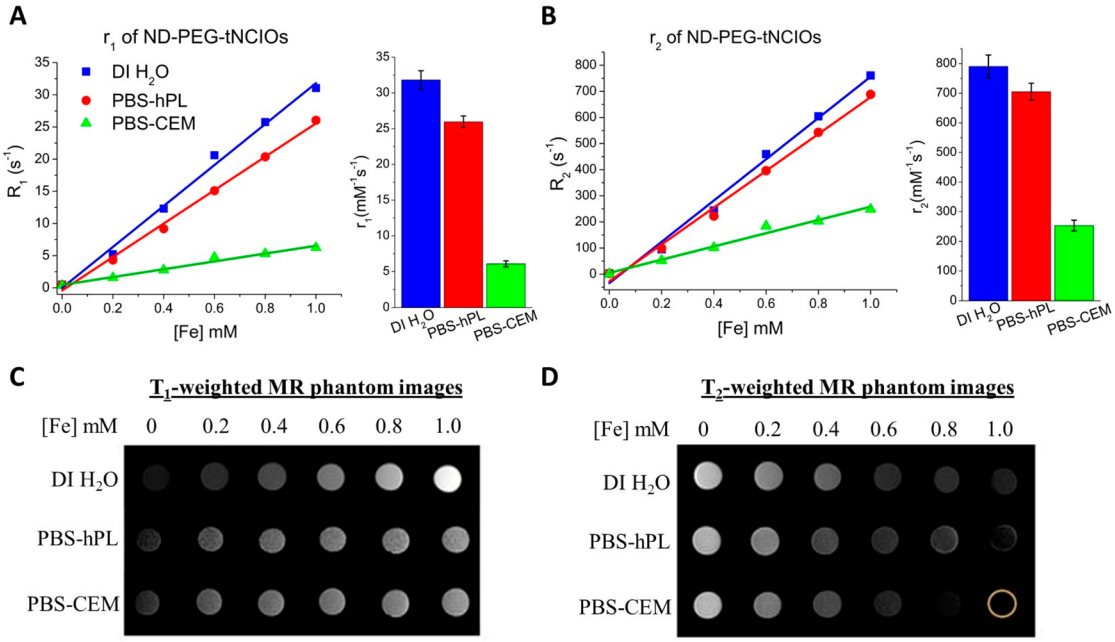

Figure 4. Magnetic resonance (MR) relaxivities measurements. (A) The R_1 vs [Fe] and (B) R_2 vs [Fe] plots of ND-PEG-tNCIOs in DI H_2O, PBS-hPL, and PBS-CEM with their respective r_1 and r_2 values in the bar diagrams to the right. (C) T_1-weighted and (D) T_2-weighted MR phantom images.

particle yields the highest increase in surface-to-volume ratio for its reduction in per unit dimension when compared to their spherical, rod-shaped, and pyramidal counterparts. On the basis of these facts, we assume that there exists more than 38.6% of the total spins as surface canted spins in tNCIOs.[46]

Figure 3C represents the temperature-dependent dc magnetometry, i.e. the field-cooled (FC) and zero-field-cooled (ZFC) magnetization measured at 50 Oersted from 10 to 325 K. By comparing the $M_{ZFC}(T)$ curves of both samples, we observed the rapid increase in moment $M_{ZFC}(T)$ and the shift in blocking temperature (T_B) to 255 K for ND-PEG-tNCIOs due to the minimal interparticle dipole interaction. We further calculated the anisotropy energy to be 8.795×10^{-20} J (see the Supporting Information) associated with ND-PEG-tNCIOs. It is also observed that the T_B coincides with the branching temperature (T_{bra}), below which nanoparticles show thermodynamic equilibrium properties and yield superparamagnetism. No T_B was observed in tNCIOs within 325 K, which is due to the higher anisotropy energy and the interparticle interaction. In addition, the nuance exchange bias observed in hysteresis $M(H)$ loop is believed to be responsible for the higher blocking temperature in tNCIOs. The $M_{FC}(T)$ curves (Figure 3D) show that the tNCIOs and ND-PEG-tNCIOs achieve the maximum magnetization at 216 and 223 K, respectively, known as the saturation temperature (T_{sat}). After T_{sat}, the spins gradually start freezing to 10K showing spin glass-like behavior. This behavior is attributed to the freezing of disordered surface spins.[46]

MR Dual Relaxivities and (T_1- and T_2-Weighted) Phantom Images. The small nanoparticles in the paramagnetic regime (sub-10 nm) significantly affect the spin–lattice (T_1) relaxation due to their prolific surface metal ions and the spins canting, while the larger ones (in the superparamagnetic regime) affect the spin–spin (T_2) relaxation due to their higher saturation magnetization.[47] However, the nanoparticles with size in the frontier of the paramagnetic and superparamagnetic regime can significantly affect both T_1 and T_2 relaxations. On the basis of this rationale, we limit the size of nanoparticles close to sub-10 nm (e.g., 12 nm), which exhibits subtle paramagnetic behavior in addition to the superparamagnetic one. Utilizing these magnetic behaviors, morphological geometry, and the conformation of the functionalized surface ligand, the nanoparticles are susceptible to enhance the dual MR (T_1 and T_2) relaxations.

We have carried out MR longitudinal relaxivity (r_1) and transverse relaxivity (r_2) measurements of ND-PEG-tNCIOs for the evaluation of their MRI performance. We selected three different media, deionized water (DI H_2O), PBS 7.4 with 10% human platelet lysate (hPL), and PBS 7.4 with CCRF-CEM cells denoted as DI H_2O, PBS-hPL, and PBS-CEM, respectively. Since PBS is a physiological buffer, the combination of hPL and CCRF-CEM cells mimics in vitro normal vascular and carcinoma environments. Figure 4A,B represents the linear plots of longitudinal and transverse relaxation rates (R_1 and R_2) vs [Fe] in those media along with their respective relaxivity bar diagrams. The ND-PEG-tNCIOs exhibit an enhanced relaxivity of r_1 = 31.82 ± 1.29, 25.96 ± 0.82, and 6.08 ± 0.46 mM^{-1} s^{-1} and r_2 = 790.58 ± 38.39, 704.98 ± 28.92, and 253.34 ± 18.16 mM^{-1} s^{-1} in DI H_2O, PBS-hPL, and PBS-CEM, respectively, at 1.41 T at 30 °C. The details of the calculated regression values are tabulated in Table 1. Although the linear plot (R_2 vs [Fe]) of DI H_2O appears to intersect at negative R_2 at [Fe] = 0, signifying the negative natural relaxation of water protons, the recorded R_2

Table 1. Comparison of r_1, r_2, r_2/r_1, and Their Regression Values

medium	r_1 (mM^{-1} s^{-1})	R^2	r_2 (mM^{-1} s^{-1})	R^2	r_2/r_1
DI H_2O	31.82 ± 1.29	0.992	790.58 ± 38.39	0.991	~25
PBS-hPL	25.96 ± 0.82	0.995	704.98 ± 28.92	0.992	~27
PBS-CEM	6.08 ± 0.43	0.976	253.34 ± 18.16	0.975	~42

DOI: 10.1021/acsabm.8b00016
ACS Appl. Bio Mater. 2018, 1, 79–89

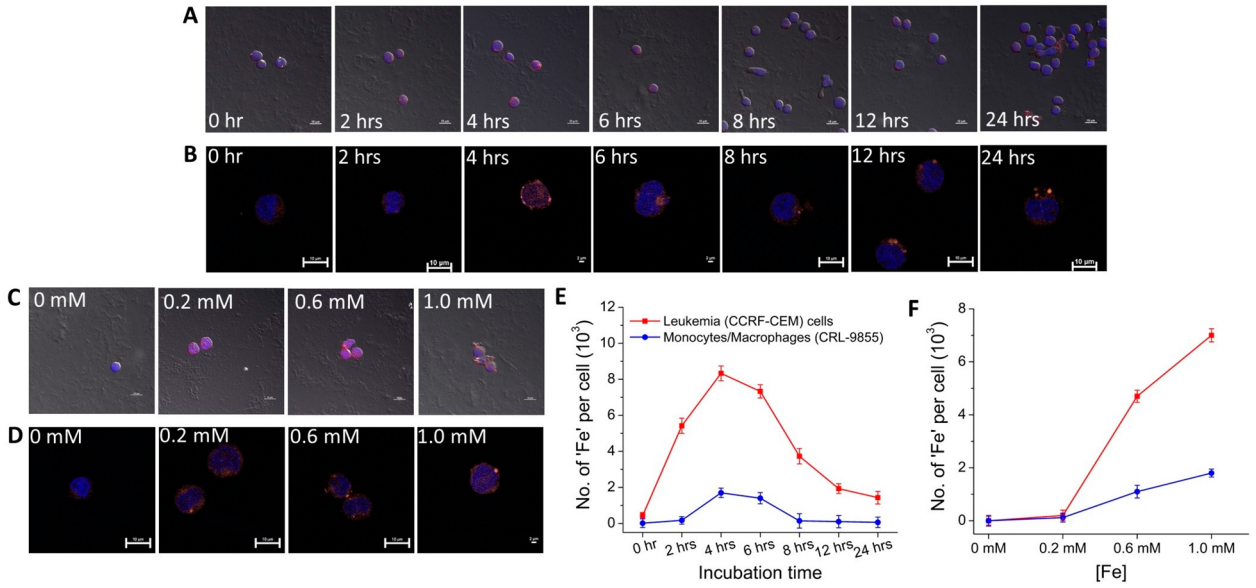

Figure 5. Fluorescence confocal microscopy (FCM) images and cellular uptake kinetics of the internalized ND-PEG-tNCIOs-(AF555Cdv) in (A) leukemia (CCRF-CEM) cells and (B) monocytes/macrophages (CRL-9855), incubated with 1 mM [Fe] for different incubation times (scale bar at 10 μm in panel A and at 2 μm for 4 and 6 h and the rest at 10 μm in panel B), and (C) leukemia (CCRF-CEM) cells and (D) monocytes/macrophages (CRL-9855), incubated with different [Fe] for 4 h (scale bar at 10 μm in panel C and scale bar at 2 μm for 1.0 mM and the rest at 10 μm in panel D). The Alexa Fluor 555 Cadaverine was adsorbed to ND-PEG-tNCIOs (bright orange); the nuclei were stained with DAPI (blue). (E) Cellular uptake as the function of incubation time. (F) Cellular uptake as the function of [Fe] in CCRF-CEM and CRL-9855.

value was 2.81334 s^{-1}. This negative intercept is attributed to an artifact of the linear regression. We further performed the in vitro T_1- and T_2-weighted MR phantom image acquisition in those media (Figure 4C,D) that show that the ND-PEG-tNCIOs can produce significantly enhanced T_1- and T_2-weighted contrasts.

The higher metal exposure or metal-rich surfaces of the nanoparticles largely promotes the water molecules' (protons) coordination and chemical exchange and hence primarily contribute to the enhancement of T_1 relaxation.[48,49] This is accompanied by the dipolar and scalar coupling of the unpaired electron spins of nanoparticles with the protons' spins by direct energy exchange in the first hydration layer (inner sphere) (Figure S3 in the Supporting Information) as described by the Solomon−Bloembergen−Morgan (SBM) theory.[50] The truncated cubic iron oxide nanoparticles possess Fe_3O_4 (100) (the basal plane), Fe_3O_4 (110), and Fe_3O_4 (111) crystal facets (Figure S4 in the Supporting Information), which consist of abundant Fe ions. According to our calculation (using materials studio software), the packing densities of Fe ions in the respective crystal facets are ~6, 8, and 14 per nm^2. This suggests that the presence of the truncated facets, i.e., (110) and (111), is advantageous for the enhancement of the T_1 relaxation. This enhancement of T_1 relaxation is also due to the vast number of canted spins present on the surface of tNCIOs. It has been reported that the canted spins may not directly contribute to the enhancement of the T_1 relaxation but is often applied to explain T_1 contrast effect in small-sized magnetic nanoparticles.[51] However, this effect is also likely accountable for the T_1 relaxation enhancement. However, the rudimentary mechanism of it is to be understood yet.

We have observed that the r_1 value decreases in heterogeneous bound media, PBS-hPL and PBS-CEM, compared to DI water. These values are contradictory as the bound medium slows down the rotational correlation time (τ_R) or the molecular tumbling rate (Figure S5 in the Supporting Information) of the ND-PEG-tNCIOs and should increase the r_1 value.[52] However, the greater water coordination number and the fast water exchange rate (inverse of exchange-correlation time, τ_m) also directly affect the r_1 values[53] in these media. Furthermore, we observed that the Flory radius of the PEG (~5 nm) is higher than the inter ligand distance (D) (~2 nm) (see calculations in the Supporting Information), which indicates that the conformation of the PEG is brush-like (Figure S3 in the Supporting Information). The brush-like conformation also promotes the faster water exchange rate in the media to contribute to the T_1 relaxation enhancement.

In addition to the enhancement of protons' T_1 relaxation, we also observed a similar effect on protons' T_2 relaxation in these media. In this study, the area of tNCIO with an average edge length of 12 nm that possess an effective diameter of ~21 nm can be extended in the medium and hence having a greater perturbation of water protons than that in the spherical nanoparticles with a similar volume. Thus, the anisotropic-shaped nanoparticles are superior to the isotropic, i.e., spherical, nanoparticles in terms of the enhancement of r_2 due to their larger effective diameter. Moreover, a large M_s of tNCIOs can induce a strong local magnetic field inhomogeneity or gradient in their local environment perturbing the transverse spin coherence, according to the quantum mechanical outer-sphere theory,[54] which in turn enhances the T_2 relaxation resulting in a high r_2 value. The D_{hyd} of ND-PEG-tNCIOs is 53 nm, which is larger than 40 nm. This indicates that the T_2 effect arises at the static dephasing regime (SDR), yielding the highest r_2 values,[55] as given by the following expression:

$$r_{2(SDR)} = \frac{2\pi\mu_0 v\gamma M_s}{9\sqrt{3}} \quad (1)$$

DOI: 10.1021/acsabm.8b00016
ACS Appl. Bio Mater. 2018, 1, 79−89

Here v is the molar volume of "Fe", $\gamma = 2.67513 \times 10^8$ rad s^{-1} T^{-1} is the gyromagnetic factor of the proton, $\mu_0 = 4\pi \times 10^{-7}$ T mA^{-1} is the magnetic permeability in a vacuum, and M_s is the saturation magnetization. Overall, we observed that the T_2-dominated character prevails in ND-PEG-tNCIOs as $r_2/r_1 \gg 6$ (Table 1), which is the hallmark feature of iron oxide nanoparticles. Also, the r_2/r_1 ratio is much higher in PBS-CEM and PBS-hPL than in the DI water with the respective values of ~42, 27, and 25, which is evident from the stronger contrast in phantom images of PBS-CEM and PBS-hPL than in that of DI H_2O (Figure 4C,D). The change in the r_2 value in different media is ascribed to the variation in diffusivity of water protons in those media. We calculated the translation diffusivity (D) values of DI H_2O, PBS-hPL, and PBS-CEM using the relation $D = k_BT/6\pi\eta r$, where η is the viscosity of the medium and r is the radius of the nanoparticle. The respective D values were determined as 2.65×10^{-11}, 1.76×10^{-11}, and 1.89×10^{-11} for the viscosity of 7.972×10^{-4}, 11.95×10^{-4}, and 11.14×10^{-4} kg/ms at 30 °C. Here, the PBS-hPL and PBS-CEM give a nearly equal but lower diffusivity, where the water protons can spend a longer period closely in the field gradient of the tNCIOs core allowing more effective dephasing of proton spins,[56] thereby enhancing the T_2 relaxation. However, the absolute r_2 values decrease in those media, which can be ascribed to the interaction of ND-PEG-tNCIOs with the lysins and to the cell growth factors present in hPL. Also, the strong cellular uptake of the nanoparticles can substantially decrease the r_2 values, as reported previously.[57] In fact, the cancer cells have an EPR effect to the nanoparticles and hence show the tendency of uptake and retention of nanoparticles.[58]

Cellular Uptake Kinetics and Immune Evasion Study. The cellular uptake or internalization and the immune evasion properties are crucial factors that determine the biological fate of the nanoparticles.[59−61] Here, we investigated the cellular uptake kinetics of ND-PEG-tNCIOs in cancerous, CCRF-CEM (i.e., human acute lymphoblastic Leukemia) cells and phagocytic, CRL 9855 (i.e., human peripheral blood monocytes/macrophages) cells. Although the positive charges on the nanoparticles improve the imaging, gene transfer, and drug delivery efficiency, they are susceptible to produce a higher toxicity[62] and the study of the role of negative charges on cellular interaction is currently of great concern. In this study, the fluorescence dye (Alexa Fluor 555 Cadaverine (AF555Cdv)) was physically adsorbed on negatively charged ND-PEG-tNCIOs after the synthesis procedure. Despite the presence of the diamine-containing AF555Cdv, the adsorbed ND-PEG-tNCIOs-(AF555Cdv) exhibits negative ζ potential in DI water.

The presence of the prolific anionic surface charge enabled us to study the charge-mediated uptake or internalization mechanisms of the nanoparticles, and the cell fluorescence from adsorbed AF555Cdv allowed us to quantify the internalized nanoparticles. Figure 5 shows the fluorescence confocal microscopy (FCM) images and uptake kinetics plots of CCRF-CEM and CRL-9855 cells incubated with ND-PEG-tNCIOs-(AF555Cdv) for different times (Figure 5A,B) and [Fe] (Figure 5C,D). The blue fluorescence is produced by the nucleus stained with DAPI while the dark orange fluorescence is produced by ND-PEG-tNCIOs-(AF555Cdv). From the images, we noticed that the nanoparticles were efficiently internalized in the CCRF-CEM cells and mostly were located at the cytoplasm or perinuclear region; however, in the case of the CRL-9855, most of the nanoparticles remained near the cell membrane. We used the ICP-OES technique to quantify the uptaken or internalized nanoparticles. According to Figure 5E, the uptake of the nanoparticles significantly increased for 4 h of incubation in both CCRF-CEM and CRL-9855 and gradually decreased for higher incubation times. Also, the uptake rate was the highest for 2 h of incubation in CCRF-CEM cells, which agrees with the uptake rate of transferrin-coated gold nanoparticles in HeLa cells,[63] while the highest uptake rate was observed between 2 and 4 h of incubation in CRL-9855. Figure 5F shows the concentration dependence of the cellular uptake of the nanoparticles for 4 h of incubation where both types of cells exhibit the highest amount of Fe uptake while incubating with 1 mM of [Fe].

Although the electrostatic force of repulsion that exists between the anionic nanoparticles and the negatively charged cell membrane prevents the internalization of the nanoparticles,[63] the minimal uptake by the CRL-9855 indicates that the anionic nanoparticles were uptaken via phagocytosis. We assume that the endocytosis of the nanoparticles by CCRF-CEM cells was mediated through micropinocytosis. The assumption was made based upon the sizes of the endocytic vesicles, clathrin (~120 nm), clathrin/caveolae-independent (~90 nm), and caveolae (~60 nm)[64] as D_{hyd} of the nanoparticles is less than 100 nm. Several groups have reported on the clathrin-mediated[65] and clathrin/caveolae-independent[66] endocytosis of anionic nanoparticles. In both observations, the CCRF-CEM cells showed a greater extent of nanoparticles uptake than those observed in CRL 9855 cells, which suggests that the endocytosis of the nanoparticles by cancerous cells dominates the phagocytosis by the phagocytic cells. Generally, the shape of the nanoparticles plays a crucial role in their cellular uptake. The oblate-shaped nanoparticles showing a lower uptake by macrophages[67] and elongated iron oxide nanoparticles with a lower uptake by the mononuclear phagocytic system (MPS) were reported.[68] Similarly, the enhanced tumor targeting ability in elongated assembly of iron oxide nanoparticles (nanoworms) than that of spherical iron oxide nanoparticles due to enhanced multivalent interaction between the nanoworms and cell receptors was reported.[69] In this study, we believe that the tNCIOs can provide higher surface contacts to the CCRF-CEM cells receptors to enhance the uptake kinetics because of their higher surface to volume ratio. Further investigation on the shape-dependent cellular uptake of iron oxide nanoparticles is currently in progress and will be reported.

CONCLUSIONS

The surface-to-volume ratio of single domain iron oxide nanoparticles, at dimensions below 12−10 nm, becomes so high so that the paramagnetic behavior gradually evolves, diminishing the superparamagnetic behavior due to the massive number of canting electron spins on the surface, as observed in this study. This subtle paramagnetic behavior, which arises from exposed Fe atoms on truncated crystal facets and brush-like PEG conformation in ND-PEG-tNCIOs, accounts for the spin−lattice relaxation time (T_1) shortening via active coupling with water protons. The observed saturation magnetization is large enough to create strong local magnetic susceptibility gradients or field inhomogeneity, and the large effective radius of cubic nanoparticles can perturb a larger number of water molecules effectively distorting the protons' spin coherence and accelerating the T_2 relaxation.

DOI: 10.1021/acsabm.8b00016
ACS Appl. Bio Mater. 2018, 1, 79−89

These nanoparticles are substantially internalized into cancerous cells and show minimal phagocytosis in CRL-9855 indicating strong immune evasiveness, thus establishing them as promising candidates for MRI dual contrast enhancement applications. The approach and results presented here provide the scientific basis for the development of single core dual modal MRI contrast agents suitable for preclinical applications, which will be superior to the hybrid nanoparticle-based dual contrast agents.

EXPERIMENTAL SECTION

Synthesis of the Nitrodopamine (ND). The nitrodopamine (ND) was synthesized following the previously reported methods[34] with slight modifications. In general, 20 g of dopamine hydrochloride and 25 g of sodium nitrite ($NaNO_2$) were dissolved in 750 mL of DI water in a 2 L conical flask, and the mixture was cooled to less than 10 or ~0 °C using an ice bath. Under constant vigorous stirring, 100 mL of 20% (v/v) sulfuric acid was added dropwise to the cooled solution under isothermal conditions. The mixture was slowly warmed to room temperature by removing it from the ice bath and kept stirring overnight at room temperature. After filtration, a yellow precipitate was obtained and was washed excessively with ice-cold water and once each with MeOH and a 50:50 mixture of EtOH/Et_2O. The washed product was vacuum-dried. The obtained moderate yellow colored powder was 6-nitrodopamine-hemisulfate (ND-HSO_4) (Figure S6A in the Supporting Information). The powder was stored at 4 °C, covered with aluminum foil until used. (The FTIR spectra are shown in Figure S7, and NMR spectra are shown in Figures S8 and S9 in the Supporting Information.)

Synthesis of the Nitrodopamine-PEG-Methoxy (ND-PEG). The peptide-coupling reaction[70] mediated with COMU was used for the synthesis of ND-PEG. The details are schematically shown in Figure S6B in the Supporting Information. A total of 1 g of MeO-PEG-COOH was dissolved in 6 mL of DMF in a conical flask. At room temperature, the solution was preactivated by adding 128 mg of COMU for 30 min via gentle shaking. The solution was then purged with nitrogen gas for 20 min and cooled to 4 °C in an ice bath (but not allowed to freeze). This solution was labeled as solution A. In the 8 mL glass vial covered with aluminum foil, 48 mg of ND-HSO_4 was dissolved in 400 μL of DMF, and 51.4 μL of NMM was added. This solution was labeled as solution B. After 10 min, solution B was added dropwise to solution A at 4 °C under nitrogen. The mixture was warmed to room temperature slowly and was shaken gently for 48 h in an incubator. HCl (18 mL, 3 M) was added to the mixture, and it was washed three times using 20 mL of chloroform in a separatory funnel, and a rotary evaporator was used to eliminate the remaining chloroform in the mixture. Finally, a pale yellow dry powder, ND-PEG-OMe, was obtained and was stored at 4 °C covered with aluminum foil until used. (FTIR and NMR spectra are shown in Figures S7 and S10, respectively, in the Supporting Information.)

Synthesis of the Truncated Cubic Iron Oxide Nanoparticles (tNCIOs). The tNCIOs were synthesized by the thermal decomposition method[15] with minor modifications. In general, 480 μL (1.5 mmol) of oleic acid (OA) and 2.7 g (3 mmol) of iron oleate were dissolved in 45 mL of *n*-trioctylamine (TOA) in a 3-neck round-bottom flask via bath sonication. The solution was degassed for half an hour and placed under nitrogen, and then the solution was heated to 340 °C at the heating rate of 10 °C per minute. After aging for 2 h at 340 °C, the solution was cooled to room temperature. The final product was precipitated using pure ethanol and was centrifuged three times to obtain the OA-coated tNCIOs. Some fraction of OA-coated tNCIOs was further centrifuged (twice more in our case) until OA-free tNCIOs precipitated in pure ethanol to obtain their powder form for characterization, whereas the remaining fraction of them was dispersed in hexane and stored at 4 °C for further functionalization.

Synthesis of the ND-PEG Grafted tNCIOs (ND-PEG-tNCIOs). The ND-PEG-tNCIOs were synthesized following the previously reported methods[34] via "ligand exchange" and "grafting to" approach. The details are schematically shown in Figure S6C in the Supporting Information. Typically, the excess hexane was removed using a rotary evaporator, and 600 mg of OA-coated iron oxide nanoparticles (OA-IO) was dispersed in 15 mL of DMF. A total of 700 mg of ND-PEG was added to the solution, and the mixture was bath sonicated for 26 h at 37 °C. The solution was washed twice using 15 mL of hexane in a separatory funnel, and the excess hexane was evaporated. After vacuum drying, the final powder obtained was ND-PEG-tNCIOs. For the purification, the powder was dissolved in 10 mL of EtOH by gentle sonication and 10 mL of ice-cooled petroleum ether was added, which turned the solution slightly turbid. The solution was magnetically decanted in the cold environment (at 4 °C). This purification step was repeated five times, and the final purified powder was obtained after drying under a vacuum.

Synthesis of the Dye Attached ND-PEG-tNCIOs. About 10 mg of ND-PEG-tNCIOs was dispersed in 1 mL of 0.1 M MES (2-(morpholino)ethanesulfonic acid) buffer at pH = 6.0 (solution 1). The 2 mg of Alexa Fluor 555 Cadaverine (AF555Cdv) was dissolved in 1 mL of PBS 7.4 (solution 2). About 3.66 mg of EDC and then 5.5 mg of NHS were added to solution 1, and then the mixture was gently shaken for 15 min at room temperature for proper mixing. The pH of this solution was increased to 7.2 by adding PBS 7.4 (solution 3). Now, solution 2 was added to solution 3, and the reaction was allowed to take place for 24 h at 4 °C with wrapped Al foil. After the reaction, the sample was centrifuged at 3900 rpm for 15 min at 4 °C 5 times using a 10 kDa MWCO centrifuge tube. The final dry powder of AF555Cdv attached ND-PEG-tNCIOs was obtained after lyophilization and named as ND-PEG-tNCIOs-AF555Cdv. We observed that the AF555Cdv is physically adsorbed onto the nanoparticles in the PEG chain, which was verified by the UV–vis emission spectra shown in Figure S11 in the Supporting Information.

ASSOCIATED CONTENT

Supporting Information

The Supporting Information is available free of charge on the ACS Publications website at DOI: 10.1021/acsabm.8b00016.

Materials, instrumentation, schematic diagram of materials synthesis, ATR-FTIR, ^1H and ^{13}C NMR spectra, UV–vis emission spectra, TGA and DSC profiles, grafting density calculation, optical images, calculation of size of a nanoparticle, anisotropy constant, and Neél relaxation time, schematic diagram of PEG conformation and crystal facets, calculation of Flory radius, schematic diagram of hydration layers, MTS cytotoxicological cellular assay (PDF)

AUTHOR INFORMATION

Corresponding Authors

*E-mail: bibech.thapa@gmail.com, bibek.thapa@upr.edu.
*E-mail: juan.beltran.huarac@gmail.com, baristary26@gmail.com.

ORCID

Bibek Thapa: 0000-0003-3188-5270
Juan Beltran-Huarac: 0000-0003-3423-0114
Brad R. Weiner: 0000-0002-5255-1918
Gerardo Morell: 0000-0003-4787-2239

Author Contributions

B.T., D.D.D., and J.B.-H. conceived and designed the project. B.T, D.D.D., C.S.M, and N.K. performed the experiments. K.T. designed the computational crystal facets. B.T. wrote the manuscript. B.T., D.D.D., N. K., J.B.-H., W.M.J., B.R.W., and G.M. analyzed the data, reviewed, and commented on the manuscript. All authors read and approved the manuscript.

Notes

The authors declare no competing financial interest.

DOI: 10.1021/acsabm.8b00016
ACS Appl. Bio Mater. 2018, 1, 79–89

■ ACKNOWLEDGMENTS

B.T., D.D.D., and G.M. received funding from NASA Cooperative Agreement no. NNX15AK43A. C.S.M. was funded by NIH Grant no. 5T34GM007821-38. K.T. received funding from the University of Puerto Rico at Rio Piedras. J.B.-H. received funding from the NSF Cooperative Agreement no. DMR-1157490, DMR-1644779, and the State of Florida. N.K. and W.M.J. received funding from NSF Cooperative Agreement no. 1002410. B.R.W. received funding from the U54 UPR-MD Anderson Cancer Center Partnership Program (NIH National Cancer Institute Grant no. U54 CA096297/CA096300). The TEM work was performed at the Ohio University Center for Electrochemical Engineering Research that received funding from NSF Grant no. CBET-1126350. The UPR Neuroimaging and Electrophysiology Facility received funding from the NIH National Institute of General Medical Sciences Award no. P20GM103642. The authors thank Dr. Yuxuan Wang (currently at UT-Dallas) for the TEM measurements at Ohio University, Dr. Huadong Zeng for the MR phantom images at AMRIS, the UPR Materials Characterization Center for access to the FTIR facility, and Professor Ram S. Katiyar for access to the UPR PPMS research facility.

■ REFERENCES

(1) Park, S. M.; Aalipour, A.; Vermesh, O.; Yu, J. H.; Gambhir, S. S. Towards Clinically Translatable In Vivo Nanodiagnostics. *Nat. Rev. Mater.* **2017**, *2*, 17014.

(2) Wei, H.; Bruns, O. T.; Kaul, M. G.; Hansen, E. C.; Barch, M.; Wisniowska, A.; Chen, O.; Chen, Y.; Li, N.; Okada, S.; Cordero, J. M.; Heine, M.; Farrar, C. T.; Montana, D. M.; Adam, G.; Ittrich, H.; Jasanoff, A.; Nielsen, P.; Bawendi, M. G. Exceedingly Small Iron Oxide Nanoparticles as Positive MRI Contrast Agents. *Proc. Natl. Acad. Sci. U. S. A.* **2017**, *114*, 2325−2330.

(3) Sinharay, S.; Pagel, M. D. Advances in Magnetic Resonance Imaging Contrast Agents for Biomarker Detection. *Annu. Rev. Anal. Chem.* **2016**, *9*, 95−115.

(4) Xue, S.; Yang, H.; Qiao, J.; Pu, F.; Jiang, J.; Hubbard, K.; Hekmatyar, K.; Langley, J.; Salarian, M.; Long, R. C.; Bryant, R. G.; Hu, X. P.; Grossniklaus, H. E.; Liu, Z. R.; Yang, J. J. Protein MRI Contrast Agent with Unprecedented Metal Selectivity and Sensitivity for Liver Cancer Imaging. *Proc. Natl. Acad. Sci. U. S. A.* **2015**, *112*, 6607−6612.

(5) Terreno, E.; Castelli, D. D.; Viale, A.; Aime, S. Challenges for Molecular Magnetic Resonance Imaging. *Chem. Rev.* **2010**, *110*, 3019−3042.

(6) Hasebroock, K.; Serkova, N. J. Toxicity of MRI and CT Contrast Agents. *Expert Opin. Drug Metab. Toxicol.* **2009**, *5*, 403−416.

(7) Kanal, E.; Tweedle, M. F. Residual or Retained Gadolinium: Practical Implications for Radiologists and Our Patients. *Radiology* **2015**, *275*, 630−634.

(8) McDonald, R. J.; McDonald, J. S.; Kallmes, D. F.; Jentoft, M. E.; Murray, D. L.; Thielen, K. R.; Williamson, E. E.; Eckel, L. J. Intracranial Gadolinium Deposition after Contrast-enhanced MR Imaging. *Radiology* **2015**, *275*, 772−782.

(9) Wagoner, M. V.; Worah, D. Gadodiamide injection: First Human Experience with the Nonionic Magnetic Resonance Imaging Enhancement Agent. *Invest. Radiol.* **1993**, *28*, S44−S48.

(10) Balakrishnan, V. S.; Rao, M.; Kausz, A. T.; Brenner, L.; Pereira, B. J. G.; Frigo, T. B.; Lewis, J. M. Physicochemical Properties of Ferumoxytol, A New Intravenous Iron Preparation. *Eur. J. Clin. Invest.* **2009**, *39*, 489−96.

(11) Singh, A.; Patel, T.; Hertel, J.; Bernardo, M.; Kausz, A.; Brenner, L. Safety of Ferumoxytol in Patients with Anemia and CKD. *Am. J. Kidney Dis.* **2008**, *52*, 907−15.

(12) Lu, M.; Cohen, M. H.; Rieves, D.; Pazdur, D. FDA report: Ferumoxytol for Intravenous Iron Therapy in Adult Patients with Chronic Kidney Disease. *Am. J. Hematol.* **2010**, *85*, 315.

(13) Weissleder, R.; Stark, D. D.; Engelstad, B. L.; Bacon, B. R.; Compton, C. C.; White, D. L.; Jacobs, P.; Lewis, J. Superparamagnetic Iron Oxide: Pharmacokinetics and Toxicity. *AJR, Am. J. Roentgenol.* **1989**, *152*, 167−73.

(14) Byrne, S. L.; Krishnamurthy, D.; Wessling, M. R. Pharmacology of Iron Transport. *Annu. Rev. Pharmacol. Toxicol.* **2013**, *53*, 17−36.

(15) Zhou, Z.; Zhu, X.; Wu, D.; Chen, Q.; Huang, D.; Sun, C.; Xin, J.; Ni, K.; Gao, J. Anisotropic Shaped Iron Oxide Nanostructures: Controlled Synthesis and Proton Relaxation Shortening Effects. *Chem. Mater.* **2015**, *27*, 3505−3515.

(16) Zhao, Z.; Zhou, Z.; Bao, J.; Wang, Z.; Hu, J.; Chi, X.; Ni, K.; Wang, R.; Chen, X.; Chen, Z.; Gao, J. Octapod iron oxide nanoparticles as high performance T_2 contrast agents for magnetic resonance imaging. *Nat. Commun.* **2013**, *4*, 2266.

(17) Walter, A.; Billotey, C.; Garofalo, A.; Bouillet, C. U.; Lefèvre, C.; Taleb, J.; Laurent, S.; Elst, L. V.; Muller, R. N.; Lartigue, L.; Gazeau, F.; Flesch, D. F.; Colin, S. B. Mastering the Shape and Composition of Dendronized Iron Oxide Nanoparticles to Tailor Magnetic Resonance Imaging and Hyperthermia. *Chem. Mater.* **2014**, *26*, 5252−5264.

(18) Macher, T.; Totenhagen, J.; Sherwood, J.; Qin, Y.; Gurler, D.; Bolding, M. S.; Bao, Y. Ultrathin Iron Oxide Nanowhiskers as Positive Contrast Agents for Magnetic Resonance Imaging. *Adv. Funct. Mater.* **2015**, *25*, 490−494.

(19) Wehrli, F. W. Magnetic Resonance of Calcified Tissues. *J. Magn. Reson.* **2013**, *229*, 35−48.

(20) Ngen, E. J.; Wang, L.; Kato, Y.; Krishnamachary, B.; Zhu, W.; Gandhi, N.; Smith, B.; Armour, M.; Wong, J.; Gabrielson, K.; Artemov, D. Imaging Transplanted Stem Cells in Real Time Using an MRI Dual-Contrast Method. *Sci. Rep.* **2015**, *5*, 13628.

(21) Shin, T. H.; Choi, J. S.; Yun, S.; Kim, S.; Song, H. T.; Kim, Y.; Park, K. I.; Cheon, J. T_1 and T_2 Dual-Mode MRI Contrast Agent for Enhancing Accuracy by Engineered Nanomaterials. *ACS Nano* **2014**, *8*, 3393−3401.

(22) Cheng, K.; Yang, M.; Zhang, R.; Qin, C.; Su, X.; Cheng, Z. Hybrid Nanotrimers for Dual T_1 and T_2-weighted Magnetic Resonance Imaging. *ACS Nano* **2014**, *8*, 9884−9896.

(23) Gong, M.; Yang, H.; Zhang, S.; Yang, Y.; Zhang, D.; Li, Z.; Zou, L. Targeting T_1 And T_2 Dual Modality Enhanced Magnetic Resonance Imaging of Tumor Vascular Endothelial Cells Based on Peptides-Conjugated Manganese Ferrite Nanomicelles. *Int. J. Nanomed.* **2016**, *11*, 4051−4063.

(24) Crossgrove, J.; Zheng, W. Manganese Toxicity Upon Overexposure. *NMR Biomed.* **2004**, *17*, 544−553.

(25) Pan, D.; Schmieder, A. H.; Wickline, S. A.; Lanza, G. M. Manganese-based MRI Contrast Agents: Past, Present and Future. *Tetrahedron* **2011**, *67*, 8431−8444.

(26) Zhou, Z.; Huang, D.; Bao, J.; Chen, Q.; Liu, G.; Chen, Z.; Chen, X.; Gao, J. A Synergistically Enhanced T_1−T_2 Dual-Modal Contrast Agent. *Adv. Mater.* **2012**, *24*, 6223−6228.

(27) Xue, S.; Zhang, C.; Yang, Y.; Zhang, L.; Cheng, D.; Zhang, J.; Shi, H.; Zhang, Y. 99mTc-labeled Iron Oxide Nanoparticles for Dual-Contrast (T_1/T_2) Magnetic Resonance and Dual-Modality Imaging of Tumor Angiogenesis. *J. Biomed. Nanotechnol.* **2015**, *11*, 1027−1037.

(28) Sharma, V. K.; Alipour, A.; Erdem, Z. S.; Aykut, Z. G.; Demir, H. V. Highly Monodisperse Low-magnetization Magnetite Nanocubes as Simultaneous T_1-T_2 MRI Contrast Agents. *Nanoscale* **2015**, *7*, 10519−10526.

(29) Huang, J.; Wang, L.; Zhong, X.; Li, Y.; Yang, L.; Mao, H. Facile Non-Hydrothermal Synthesis of Oligosaccharide coated sub-5 nm Magnetic Iron Oxide Nanoparticles with Dual MRI Contrast Enhancement Effects. *J. Mater. Chem. B* **2014**, *2*, 5344.

(30) Qiao, L.; Fu, Z.; Li, J.; Ghosen, J.; Zeng, M.; Stebbins, J.; Prasad, P. N.; Swihart, M. T. Standardizing Size- and Shape-Controlled Synthesis of Monodisperse Magnetite (Fe_3O_4) Nano-

DOI: 10.1021/acsabm.8b00016
ACS Appl. Bio Mater. 2018, 1, 79−89

crystals by Identifying and Exploiting Effects of Organic Impurities. *ACS Nano* **2017**, *11*, 6370−6381.
(31) Thapa, B.; Diestra, D. D.; Huarac, J. B.; Weiner, B. R.; Morell, G. Enhanced MRI T_2 Relaxivity in Contrast-Probed Anchor-Free PEGylated Iron Oxide Nanoparticles. *Nanoscale Res. Lett.* **2017**, *12*, 312.
(32) Diestra, D. D.; Huarac, J. B.; Rincon, D. B.; Feliciano, J. A. G.; Gonzalez, C. I.; Weiner, B. R.; Morell, G. Biocompatible Zns:Mn Quantum Dots for Reactive Oxygen Generation and Detection in Aqueous Media. *J. Nanopart. Res.* **2015**, *17*, 461.
(33) Huarac, J. B.; Guinel, M. J. F.; Weiner, B. R.; Morell, G. Bifunctional Fe_3O_4/Zns:Mn Composite Nanoparticles. *Mater. Lett.* **2013**, *98*, 108−111.
(34) Lassenberger, A.; Bixner, O.; Gruenewald, T.; Lichtenegger, H.; Zirbs, R.; Reimhult, E. Evaluation of High-Yield Purification Methods on Monodisperse PEG Grafted Iron Oxide Nanoparticles. *Langmuir* **2016**, *32*, 4259−4269.
(35) Sayed, F. N.; Polshettiwar, V. Facile and Sustainable Synthesis of Shaped Iron Oxide Nanoparticles: Effect of Iron Precursor Salts on the Shapes of Iron Oxides. *Sci. Rep.* **2015**, *5*, 9733.
(36) Monazam, E. R.; Breault, R. W.; Siriwardane, R. Kinetics of Magnetite (Fe3O4) Oxidation to Hematite (Fe2O3) in Air for Chemical Looping Combustion. *Ind. Eng. Chem. Res.* **2014**, *53*, 13320−13328.
(37) Rodríguez, L. S.; Lafontaine, M. M.; Castro, C.; Vega, J. M.; Esteves, M. L.; Juan, E. J.; Mora, E.; Lugo, M. T.; Rinaldi, C. Synthesis, Stability, Cellular Uptake, and Blood Circulation Time of Carboxymethyl-Inulin Coated Magnetic Nanoparticles. *J. Mater. Chem. B* **2013**, *1*, 2807−2817.
(38) Jokerst, J. V.; Lobovkina, T.; Zare, R. N.; Gambhir, S. S. Nanoparticle PEGylation for Imaging and Therapy. *Nanomedicine* **2011**, *6*, 715−728.
(39) *Zetasizer Nano User Manual*; Malvern Instruments Ltd.: Worcestershire, U.K., 2013; 1.1, 13-3.
(40) Huang, J.; Wang, L.; Lin, R.; Wang, A. Y.; Yang, L.; Kuang, M.; Qian, W.; Mao, H. Casein-Coated Iron Oxide Nanoparticles for High MRI Contrast Enhancement and Efficient Cell Targeting. *ACS Appl. Mater. Interfaces* **2013**, *5*, 4632−4639.
(41) Park, Y.; Whitaker, R. D.; Nap, R. J.; Paulsen, J. L.; Mathiyazhagan, V.; Doerrer, L. H.; Song, Y. Q.; Hürlimann, M. D.; Szleifer, I.; Wong, J. Y. Stability of Superparamagnetic Iron Oxide Nanoparticles at Different pH Values: Experimental and Theoretical Analysis. *Langmuir* **2012**, *28*, 6246−6255.
(42) Arami, H.; Khandhar, A.; Liggitt, D.; Krishnan, K. M. In Vivo Delivery, Pharmacokinetics, Biodistribution and Toxicity of Iron Oxide Nanoparticles. *Chem. Soc. Rev.* **2015**, *44*, 8576−8607.
(43) Zhen, G.; Muir, B. W.; Moffat, B. A.; Harbour, P.; Murray, K. S.; Moubaraki, B.; Suzuki, K.; Madsen, I.; Olshina, N. A.; Waddington, L.; Mulvaney, P.; Hartley, P. G. Comparative Study of the Magnetic Behavior of Spherical and Cubic Superparamagnetic Iron Oxide Nanoparticles. *J. Phys. Chem. C* **2011**, *115*, 327−334.
(44) Smolensky, E. D.; Park, H. Y. E.; Berquo, T. S.; Pierre, V. C. *Contrast Media Mol. Imaging* **2010**, 189−199.
(45) Concha, B. M.; Zysler, R. D.; Romero, H. Anomalous Magnetization Enhancement and Frustration in the Internal Magnetic Order on $(Fe_{0.69}Co_{0.31})$ $B_{0.4}$ Nanoparticles. *Appl. Sci.* **2012**, *2*, 315−326.
(46) Coey, J. M. D. Noncollinear Spin Arrangement in Ultrafine Ferrimagnetic Crystallites. *Phys. Rev. Lett.* **1971**, *27*, 1140−1142.
(47) Gossuin, Y.; Gillis, P.; Hocq, A.; Vuong, Q. L.; Roch, A. Magnetic Resonance Relaxation Properties of Superparamagnetic Particles. *WIREs Nanomed. Nanobiotechnol.* **2009**, *1*, 299−310.
(48) Zhou, Z.; Wang, L.; Chi, X.; Bao, J.; Yang, L.; Zhao, W.; Chen, Z.; Wang, X.; Chen, X.; Gao, J. Engineered Iron-Oxide-Based Nanoparticles as Enhanced T_1 Contrast Agents for Efficient Tumor Imaging. *ACS Nano* **2013**, *7*, 3287−3296.
(49) Zhou, Z.; Zhao, Z.; Zhang, H.; Wang, Z.; Chen, X.; Wang, R.; Chen, Z.; Gao, J. Interplay between Longitudinal and Transverse Contrasts in Fe_3O_4 Nanoplates with (111) Exposed Surfaces. *ACS Nano* **2014**, *8*, 7976−7985.
(50) Solomon, I. Relaxation Processes in a System of Two Spins. *Phys. Rev.* **1955**, *99*, 559−565.
(51) Bao, Y.; Sherwood, J. A.; Sun, Z. Magnetic Iron Oxide Nanoparticles as T_1 Contrast Agents for Magnetic Resonance Imaging. *J. Mater. Chem. C* **2018**, *6*, 1280−1290.
(52) De León-Rodríguez, L. M.; Martins, A. F.; Pinho, M. C.; Rofsky, N. M.; Sherry, A. D. Basic MR Relaxation Mechanisms and Contrast Agent Design. *J. Magn. Reson. Imaging* **2015**, *42*, 545−565.
(53) Merbach, A.; Helm, L.; Tóth, É. *The Chemistry of Contrast Agents in Medical Magnetic Resonance Imaging*, 2nd ed.; John Wiley & Sons, 2013.
(54) Gillis, P.; Koenig, S. H. Transverse Relaxation of Solvent Protons Induced by Magnetized Spheres: Application to Ferritin, Erythrocytes and Magnetite. *Magn. Reson. Med.* **1987**, *5*, 323−345.
(55) Lee, N.; Yoo, D.; Ling, D.; Cho, M. H.; Hyeon, T.; Cheon, J. Iron Oxide Based Nanoparticles for Multimodal Imaging and Magnetoresponsive Therapy. *Chem. Rev.* **2015**, *115*, 10637−10689.
(56) Stephen, Z. R.; Kievit, F. M.; Zhang, M. Magnetite Nanoparticles for Medical MR Imaging. *Mater. Today* **2011**, *14*, 330−8.
(57) Martin, A. L.; Bernas, L. M.; Rutt, B. K.; Foster, P. J.; Gillies, E. R. Enhanced Cell Uptake of Superparamagnetic Iron Oxide Nanoparticles Functionalized with Dendritic Guanidines. *Bioconjugate Chem.* **2008**, *19*, 2375−2384.
(58) Kobayashi, H.; Watanabe, R.; Choyke, P. L. Improving Conventional Enhanced Permeability and Retention (EPR) Effects; What is the Appropriate Target? *Theranostics* **2014**, *4*, 81−89.
(59) Wang, G.; Inturi, S.; Serkova, N. J.; Merkulov, S.; McCrae, K.; Russek, S. E.; Banda, N. K.; Simberg, D. High-Relaxivity Superparamagnetic Iron Oxide Nanoworms with Decreased Immune Recognition and Long-Circulating Properties. *ACS Nano* **2014**, *8*, 12437−49.
(60) Huarac, J. B.; Zhang, Z.; Pyrgiotakis, G.; DeLoid, G.; Vaze, N.; Demokritou, P. Development of Reference Metal and Metal Oxide Engineered Nanomaterials for Nanotoxicology Research Using High Throughput and Precision Flame Spray Synthesis Approaches. *NanoImpact* **2018**, *10*, 26−37.
(61) Diestra, D. D.; Thapa, B.; Huarac, J. B.; Weiner, B. R.; Morell, G. L-cysteine Capped Zns:Mn Quantum Dots for Room-Temperature Detection of Dopamine with High Sensitivity and Selectivity. *Biosens. Bioelectron.* **2017**, *87*, 693−700.
(62) Fröhlich, E. The Role of Surface Charge in Cellular Uptake and Cytotoxicity of Medical Nanoparticles. *Int. J. Nanomed.* **2012**, *7*, 5577−5591.
(63) Chithrani, B. D.; Ghazani, A. A.; Chan, W. C. W. Determining the Size and Shape Dependence of Gold Nanoparticle Uptake into Mammalian Cells. *Nano Lett.* **2006**, *6*, 662−668.
(64) Conner, S. D.; Schmid, S. L. Regulated Portals of Entry into the Cell. *Nature* **2003**, *422*, 37−44.
(65) Lai, S. K.; Hida, K.; Man, S. T.; Chen, C.; Machamer, C.; Schroer, T. A.; Hanes, J. Privileged Delivery of Polymer Nanoparticles to the Perinuclear Region of Live Cells via a Non-Clathrin, Non-Degradative Pathway. *Biomaterials* **2007**, *28*, 2876−2884.
(66) Frenkel, O. H.; Debotton, N.; Benita, S.; Altschuler, Y. Targeting of Nanoparticles to the Clathrin-Mediated Endocytic Pathway. *Biochem. Biophys. Res. Commun.* **2007**, *353*, 26−32.
(67) Toy, R.; Peiris, P. M.; Ghaghada, K. B.; Karathanasis, E. Shaping Cancer Nanomedicine: The Effect of Particle Shape on the In Vivo Journey of Nanoparticles. *Nanomedicine (London, U. K.)* **2014**, *9*, 121−134.
(68) Champion, J. A.; Mitragotri, S. Role of Target Geometry in Phagocytosis. *Proc. Natl. Acad. Sci. U. S. A.* **2006**, *103*, 4930−4934.
(69) Park, J. H.; Maltzahn, G. V.; Zhang, L.; Schwartz, M. P.; Ruoslahti, E.; Bhatia, S. N.; Sailor, M. J. Magnetic Iron Oxide Nanoworms for Tumor Targeting and Imaging. *Adv. Mater.* **2008**, *20*, 1630−1635.

DOI: 10.1021/acsabm.8b00016
ACS Appl. Bio Mater. 2018, 1, 79−89

(70) d'Amour, J.; Twibanire, K.; Grindley, T. B. Efficient and Controllably Selective Preparation of Esters Using Uronium-Based Coupling Agents. *Org. Lett.* **2011**, *13*, 2988−2991.

DOI: 10.1021/acsabm.8b00016
ACS Appl. Bio Mater. 2018, 1, 79−89